Free-Flight Aerodynamic Testing of the Skylon Spaceplane

Andrew Hyslop * , Luke J. Doherty † and Matthew McGilvray ‡
Oxford Thermofluids Institute, University of Oxford, Oxford, United Kingdom, OX2 0ES

Andrew Neely § and Liam P. McQuellin ¶
University of New South Wales, Canberra, Australia, 2600

James Barth‖ and Gerrie Mullen **
Reaction Engines Limited, Abingdon, United Kingdom, OX14 3DB

The determination of aerodynamic coefficients for complex high speed vehicles still requires experimental measurement. This paper details the development of the free-flight measurement technique within the University of Oxford High Density Tunnel (HDT). In particular, a novel image processing technique is developed for calculating the position of the model from high speed video. This study focusses on the measurement of high Reynolds number experimental aerodynamic data for a subscale model of Reaction Engines' Skylon spaceplane. Testing was undertaken at a Mach 7 test condition replicating flight at an altitude of 63.5 km. Results for lift, drag and pitching moment coefficient were obtained over a range of angles of attack. Lift coefficient was nearly linear over the range of angles of attack tested and drag coefficient was parabolic in shape but sensitive to model yaw. The vehicle was also shown to be statically unstable, a common characteristic of canard configuration vehicles.

Nomenclature

c = reference length (m)

m = mass (kg)

n = scaling factor

p = roll rate (body axis) (rads^{-1})

q = pitch rate (body axis) (rads^{-1})

$\overline{q}$ = dynamic pressure (Pa)

r = yaw rate (body axis) (rads^{-1})

*D.Phil. Candidate, Department of Engineering Science
†Senior Research Associate, Department of Engineering Science, AIAA Member
‡Associate Professor, Department of Engineering Science
§Professor, School of Engineering and Information Technology, AIAA Associate Fellow
¶Research Engineer, School of Engineering and Information Technology, UNSW Canberra, AIAA Member
‖Lead Aerodynamicist
**Vehicle Studies Manager

x, y, z = displacement (m)

$\ddot{x}, \ddot{y}, \ddot{z}$ = acceleration (ms^{-1})

C_D = drag coefficient

C_L = lift coefficient

C_M = pitching moment coefficient

D = drag (N)

I = moment of inertia (kgm^2)

L = lift (N)

M = pitching moment (Nm)

M_∞ = freestream Mach number

P = pressure (Pa)

R = gas constant ($Jkg^{-1}K^{-1}$)

Re_L = Reynolds number (based on vehicle length)

S = reference area (m^2)

T = temperature (K)

U = uncertainty

U_∞ = freestream velocity (ms^{-1})

γ = ratio of specific heats

θ = pitch angle (Euler) (°)

μ = dynamic viscosity (Pas)

ρ = density (kgm^{-3})

ϕ = roll angle (Euler) (°)

ψ = yaw angle (Euler) (°)

Subscripts

$_{cg}$ = centre of gravity

$_f$ = fluid

$_m$ = model

$_v$ = vehicle

$_\infty$ = freestream

$_0$ = total

I. Introduction

REUSABLE single-stage-to-orbit (SSTO) spaceplanes have the potential to revolutionise the cost of orbital access. However, this requires a vehicle design that can perform over a range of flight regimes, as the vehicle takes off like a conventional aeroplane and accelerates from the subsonic regime to the hypersonic regime, carrying a payload to low Earth orbit (LEO) before returning to land.

Currently, there is little numerical or experimental aerodynamic performance data for spaceplanes, particularly at hypersonic Mach numbers. Furthermore, due to the length of spaceplanes, boundary layer transition is expected to occur on the vehicle which is difficult to predict computationally [1] [2]. In general, the creation of a high-fidelity, nose-to-tail numerical simulation of hypersonic vehicles is difficult and computationally expensive. Validation of such simulations requires high-quality experimental data.

A substantial amount of existing spaceplane research was conducted during the National Aero-Space Plane (NASP) programme (1986-1995). Phillips [3] conducted sting mounted aerodynamic tests for the Test Technique Demonstrator, a generic spaceplane geometry used in the development of NASP. Forces were measured using a six component strain-gauge balance at a range of hypersonic Mach numbers. In parallel, significant advancements were made in the development of computational models for spaceplanes during this period, however, there were high uncertainties in the laminar-turbulent transition location in the high Mach number regime [4]. The programme was ultimately terminated due to the increasing costs of achieving SSTO at the time.

Skylon, a SSTO spaceplane currently in development by Reaction Engines Ltd. (REL), utilises SABRE engines which harness state-of-the-art pre-cooler technology to enable the engine to remain air-breathing at altitudes up to 26 km at Mach 5, before transitioning to rocket mode [5]. Mehta *et al.* [6] conducted numerical simulations using NASA's Cart3D software to investigate the Skylon airframe aerodynamics for powered flight and assess the plume impingement from the SABRE engines on the aft fuselage for potential thermal-structural issues. The results showed that at Mach numbers above 8.5, the under-expanded plumes had a favourable effect on the aerodynamic coefficients causing divergence from in-house REL predications. Mehta provides the only source for information of trajectory points and aerodynamic coefficients of Skylon in open literature. However, there is a lack of experimental data that validate these numerical simulations.

This paper presents an experimental investigation of the aerodynamic performance of the Skylon vehicle through the development of the free-flight experimental technique in the Oxford High Density Tunnel (HDT), thereby creating an experimental aerodynamic coefficient database for Skylon at high Mach numbers which can be used to validate numerical data. Free-flight experiments require the model and flow conditions to be suitably scaled so that the dynamics and aerodynamics of the sub-scale model are representative of flight conditions. For spaceplanes, flight representative conditions are particularity important due to the sensitivity of aerodynamic coefficients to the position of boundary layer transition over the body of the vehicle. Aerodynamic data at a range of angles of attack was acquired using both

image tracking on high speed videos and an on-board Inertial Measurement Unit (IMU). This work represents the first experimental investigation of the aerodynamics of Skylon at high Mach number flight conditions. Section II of the paper describes the Free-flight technique as implemented in the HDT. Section III details the experimental set up, model design and the application of the scaling laws. Section IV discusses the data processing used to obtain aerodynamic coefficients. Section V presents the results of the experiments.

II. Free-Flight Technique and Scaling

There are many difficulties associated with measuring aerodynamic forces in hypersonic facilities. Conventional methods typically include the use of a sting to rigidly mount a sub-scale model with aerodynamic forces and moments measured through the use of a multicomponent force balance. The presence of the sting, however, results in undesirable drag and also produces unrealistic flow fields downstream of the model. Pick [7] showed that the interference effects of a sting is very influential at angles of attack of 15 degrees or greater for sharp cones in hypersonic flow. Additionally for sting mounted models, it is important that the dynamic response of the model and balance upon application of transient loads is shorter than the useful test time to allow for the measurement of quasi-static aerodynamic forces. This design criteria can often be difficult to achieve in short duration hypersonic facilities [8].

The free-flight technique discards the sting and allows the model to move unconstrained in the flow in six degrees of freedom [9]. A typical methodology of a free-flight test in short duration facilities is as follows: the model is released prior to arrival of the test flow, the flow is initiated over the model which allows it to move as it would in flight. Consequently, there is no external interference on the flow around the model, thus, it is more representative of real flight. This technique requires non-intrusive methods to measure accelerations, from which the aerodynamic forces may be derived. Measurement of acceleration can be achieved using two different methods: On-board accelerometers and gyroscopes, and image tracking of the vehicle's position from high speed videos. The free-flight technique has been successfully applied in short-duration hypersonic test facilities by several authors. Mudford [10] measured 6 degrees of freedom movement on a steel hemispherical-nosed cylinder using accelerometers and gyroscopes. This work was continued by Kennell *et al.* [11, 12] using ESA's HEAXFLY INT EFTV geometry. Tanno [13] also used accelerometers to measure 6 component motion of blunted cone, capsules and lifting bodies in a free piston shock tunnel. Laurence *et al.* [14] used image tracking with sub-pixel accuracy measuring 3 component motion on the NASA Orion vehicle.

The dynamic behaviour of models in free-flight is directly related to the model geometry, test flow properties and the model mass distribution. Therefore, it is important that all aspects of the vehicle of interest and flow properties are scaled appropriately so that the data obtained from the derived model during free-flight corresponds to the full-scale vehicle behaviour when in flight. Wolowicz [15] provides a thorough derivation and discussion on scaling; a brief summary is provided here. For free-flying models there are two methods available for scaling - Froude number scaling

and Mach number scaling. Froude scaling allows for the preservation of gravitational effects acting on the model, thereby matching the kinematics of the model and maintaining angle of attack similitude. Mach scaling preserves the effects of compressibility within the flow. In this work, Mach scaling was used as all testing was conducted in the hypersonic regime where compressible effects dominate. Mach scaling requires that both the freestream Mach number and Reynolds number are matched between flight and the wind tunnel test. Matching Reynolds number preserves features such as boundary layer transition and viscous effects which are particularly important for geometries such as spaceplanes. All aspects of the vehicle's geometry are scaled by the desired factor, n, to give the model length, and the position of the centre of mass of the model for example. In practice, it is not always possible to scale all geometric aspects of the vehicle because features such as surface roughness would be required to be very fine and difficult to machine. To preserve the dynamic behaviour of the vehicle, the model's mass and moment of inertia must be scaled according to Eq. (1) and Eq. (2) where subscript m denotes the model, subscript v the full-scale vehicle and ρ_f is the fluid density.

$$\frac{m_m}{m_v} = n^3 \frac{\rho_{f,m}}{\rho_{f,v}} \tag{1}$$

$$\frac{I_m}{I_v} = n^5 \frac{\rho_{f,m}}{\rho_{f,v}} \tag{2}$$

Under the assumption of matched freestream Reynolds number and Mach number, taking ratios of Reynolds number gives:

$$\left(\frac{\rho_f T^{\frac{1}{2}}}{\mu}\right)_m = \left(\frac{\rho_f T^{\frac{1}{2}}}{\mu}\right)_v \tag{3}$$

If the model scale and vehicle trajectory point are defined, all properties on the right hand side of Eq. (3) are fixed. The left hand side therefore describes a test envelope that the facility must meet in order to achieve similitude. Once the facility conditions are chosen, Eq. (1) and Eq. (2) may be used to determine the required model mass and moment of inertia. This fully defines the model inertial specifications for dynamic similitude within the limitations of Mach scaling. High temperature effects such as flow chemistry play a secondary role in aerodynamic experiments and as a consequence, stagnation enthalpies are not replicated in Mach scaling.

III. Experimental Setup

A. Facility and Test Infrastructure

The experiments were conducted in the University of Oxford High Density Tunnel located within the Oxford Thermofluids Institute. The facility was operated as a Ludwieg tube with a Mach 7 contoured nozzle with exit diameter

350 mm, producing a core flow of 280 mm at nozzle exit. The facility currently has a maximum operational total pressure of 50 bar (which can be upgraded to 275 bar). For further details on the HDT operation and measurement of freestream conditions, see McGilvray *et al.* [16] and Wylie *et al.* [17]. This facility was selected for these experiments because it offers sufficient steady flow duration (~ 50 ms) to allow the free-flight of low inertia models through a range of attitudes at flight representative conditions.

Shown in Fig. 1, a catcher net and model drop mechanism were designed for the HDT. The catcher mechanism was designed to prevent the model from exiting the test section into the dump tank, from where it would be difficult to retrieve. The catcher mechanism was also designed to reduce the damage sustained by the model during a test. The catcher consisted of two aluminium rings with Dyneema cord of 1.5 mm diameter fed through 32 uniformly spaced holes. The upstream ring was held at a 30° inclination, with the purpose of deflecting the model towards the tunnel floor which was lined with multi-layer foam padding.

The drop mechanism was designed to release the model into the core flow prior to the arrival of test flow. The mechanism consisted of a 25 mm diameter electromagnet attached to a SMC pneumatic actuator of 50 mm stroke length. A bespoke electrical unit controls the timing of the solenoids. Upon receiving a TTL pulse from the tunnel, the box triggers the electromagnet to release the model and powers the solenoids to retract the actuator, pulling the electromagnet out of the oncoming flow. The TTL pulse timing may be varied with respect to the facility to achieve the desired time of model free-fall before flow onset. A 3D printed holder was used to house the electromagnet and set the initial angle of attack of the model. The holder shape was conformal to the Skylon model, setting and fixing the roll axis and a steel rod was connected to the holder to limit any rotations about the yaw axis. The printed holder is shaped to position the electromagnet directly above the centre of gravity of the model to minimise any exerted rotational inertia on the model when it is released and hence provided a consistent and repeatable model release.

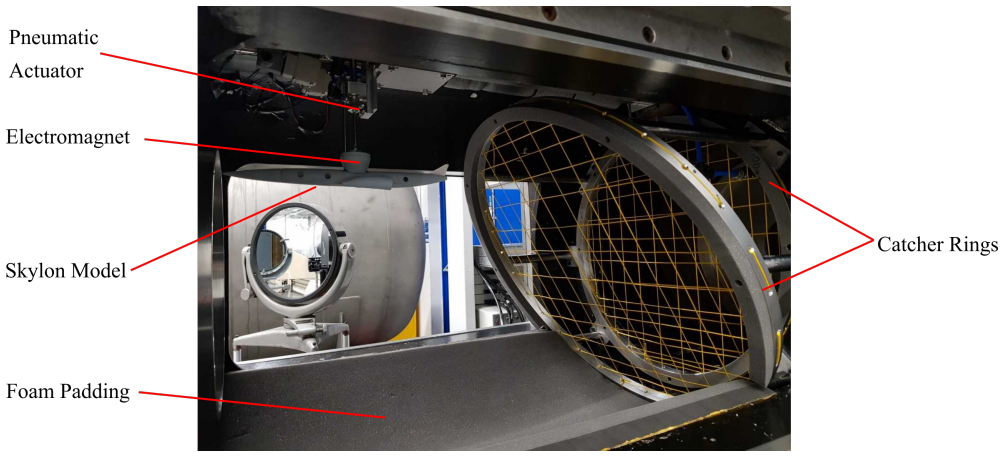

Fig. 1 Free-flight drop mechanism and catcher rings in the HDT test section.

B. Test Condition and Model Scaling

Using the scaling laws set out in Section II, Figure 2 plots the required unit Reynolds number to achieve similitude of flight conditions for a range of hypersonic vehicles over their trajectories for a given model length. The vehicle data corresponds to flight trajectory points assuming a model length of 337 mm, matching the length of model used in this work. Also plotted is the unit Reynolds number capability of the HDT for each nozzle. It can be seen from Figure 2 that dynamic similitude of spaceplanes requires large unit Reynolds numbers that are in excess of the capability of the HDT. This is a direct consequence of the significant length (on order of 80m) of this class of vehicle in comparison with the other vehicles presented.

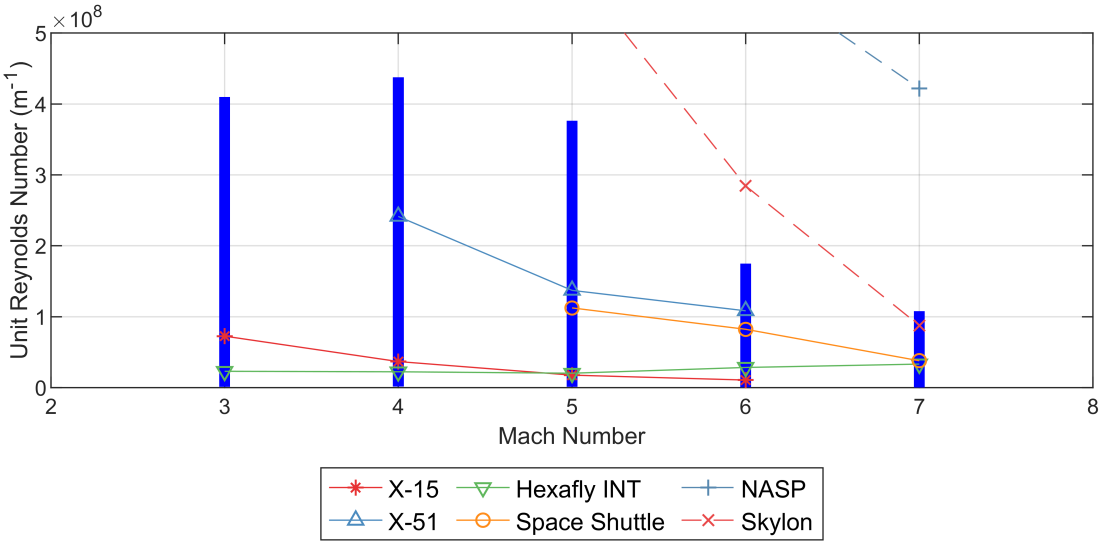

Fig. 2 Unit Reynolds number capability (blue bars) of HDT facility compared with similitude requirements of various hypersonic vehicles assuming a model length of 337 mm. Trajectory points for the vehicles are taken from [18], [19], [20], [21], [22] and [6].

For Skylon, similitude can only be achieved at Mach 7 at the upper operational limit of HDT. Figure 3 presents the variation in required flow total pressure with model length assuming Mach 7 flow and a Reynolds number of 32.3×10^6 as used by Mehta *et al.* [6] (equivalent to 42 km altitude). The variation in required model mass, calculated according to Eq. (1) is also plotted. A model length of 337 mm was chosen, corresponding to a scale of 1:240. This scale was selected so that the model would have room to manoeuvre in the core flow during the course of a test. At this scale, a total pressure of 208 bar is required to ensure similitude. Although the HDT is capable of achieving this condition, the use of free-flight at such high forces was deemed to be too risky to the tunnel infrastructure. Consequently, a reduced total pressure of 14 bar was chosen for this work, corresponding to an altitude of 63.5 km.

Table 1 compares the nominal test condition with an equivalent flight condition. Flight conditions are derived by matching the Reynolds number of the 14 bar tunnel condition at Mach 7. Viscosity was calculated using Keyes' Law

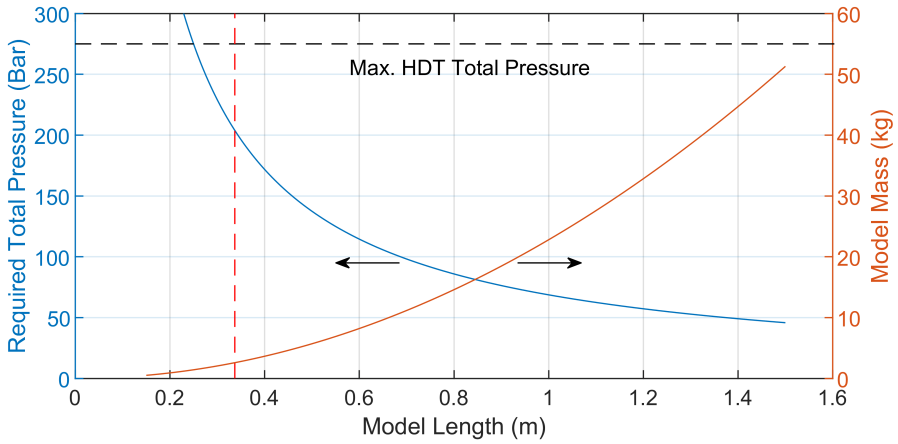

Fig. 3 Mach scaling applied to Skylon for an altitude of 42 km to match Reynolds number and mass (Mach 7, T_0 = 537 K). Red dashed line represents model length used in this work

[23] for tunnel conditions and Sutherland's Law [24] for flight. Equivalent flight conditions were calculated through US Standard Atmosphere [25]. Flight total temperature was calculated using isentropic relations with a ratio of specific heats (γ) of 1.4.

Table 2 compares the scaled inertial properties for similitude and the test model properties for the Mach 7 test condition. The vehicle mass includes the fuel load and is taken from the Mach 7, 42 km altitude condition. Moment of inertia was predicted using CAD software for the model. The position of the centre of gravity was well matched to the full-size vehicle and therefore the model gives insight into vehicle longitudinal stability. However, a lighter model was used for ease of manufacture and to prevent damage to the HDT in this proof-of-concept campaign. Consequently, model rotational and linear motion during the test will be greater than flight but the magnitude of measured aerodynamic forces are unaffected by the mass mis-match.

Table 1 Flight vs scaled tunnel condition.

	HDT Test Flow	**Flight**
Altitude (km)	63.5	63.5
Mach Number	7	7
Velocity (ms^{-1})	989.6	2181
Density (kgm^{-3})	0.022	0.00018
Static Pressure (Pa)	317.4	12.53
Total Pressure (kPa)	1331	51.88
Static Temperature (K)	49.7	241.5
Total Temperature (K)	537	2608
Dynamic Viscosity (μPas)	3.56	0.16
Unit Reynolds Number ($10^6 m^{-1}$)	6.26	0.025
Reynolds Number (10^6)	2.1	2.1

Table 2 Scaling applied to the inertial properties of Skylon.

	Full Scale	Scaled	Model	Mismatch Error
Length	81.3 m	337 mm	337 ± 0.1 mm	0 %
Mass	2.43x10^5 kg	2.03 kg	0.219 ± 0.001 kg	89.2 %
$\mathbf{X}_{cg}$	43.84 m	181.3 mm	181 ± 1 mm	0.2 %
$\mathbf{Z}_{cg}$	-0.26 m	-1 mm	-1 ± 1 mm	0 %
$\mathbf{I}_{yy}$	1.77x10^7 kgm^2	2.43x10^6 gmm^2	1.07x10^6 gmm^2	127.1 %

C. Model Design

The experimental model was geometrically scaled from the full-size vehicle, with the exception of the wings, canards and tail, which were thickened to 0.2 mm at the trailing edge to maintain sufficient rigidity. The engines were designed as if in rocket/reentry mode, i.e. closed to the oncoming flow. This increases the overall drag compared with the vehicle in air-breathing mode. Due to the small model scale, no engine plume effects were accounted for in these experiments. The model was designed to be suitable for rapid prototyping using a Polyjet Objet 30 3D printer. The vehicle was subdivided into 4 sections: nose, tail, fuselage and wings, thereby allowing for delicate features to be replaced in the case of damage during a test. Dividing the model also allowed for cavities to be created that accommodated ballast (used to locate the centre of mass) and the on-board Data Acquisition module (DAQ) and battery. The model was also designed so that the inertial measurement unit (IMU) on the DAQ was located at the centre of mass of the model to within +/- 0.1 mm. A bespoke metal plate was machined to fit the top of the model to allow compatibility with the drop mechanism electromagnet. Figure 4 shows a photograph of the final assembly. The black circles visible on the side are for image tracking of the model during free-flight.

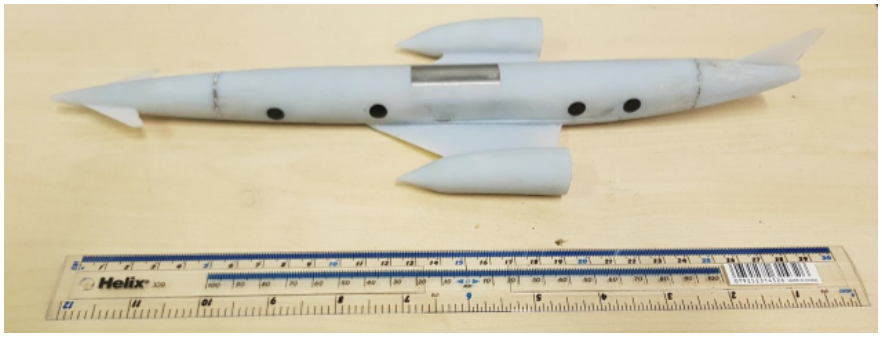

Fig. 4 Skylon scale model.

D. On-board Data Acquisition System

The on-board inertial measurement instrument (hereby referred to as the DAQ) consisted of an integrated 3-axis accelerometer and 3-axis gyroscope, non-volatile memory, a Bluetooth radio module and a microcontroller. These components were integrated on a single printed circuit board with planform dimensions of ~ 114 mm x 12 mm. This

measurement system has successfully demonstrated the ability to collect accurate acceleration and angular velocity data necessary for hypersonic wind tunnel model aerodynamics [12, 26]. The IMU was a single chip device with an accelerometer full scale range of +/- 16 g and a data output rate of 4 kHz. The full scale range of the gyroscope was +/-2000 deg/s with a data output rate of 8 kHz. Non-linearity of the accelerometer and gyroscope axis is reported to be 0.1% and 0.5% respectively. For this work a sample rate of 8 kHz was used which allowed for $\sim$ 320 samples over the 40 ms duration of the experiment. Triggering of the instrument was achieved by detection of sustained free-fall upon model release.

E. Optical Setup

For this work, the flow field was imaged using schlieren and the model movement by direct imaging using two high speed cameras. For the schlieren, a conventional Z-type setup with horizontal knife edge was used to visualise the density gradients in flow field around the Skylon model. The light was emitted continuously from a Luminous PT-120-TE green LED as the camera's detector is particularly sensitive to this wavelength region. The flow was imaged with a FASTCAM AX200 high-speed camera set to a frame rate of 6400 fps with 1,024 x 1,024 pixel resolution at a focal length of 130 mm which fully encapsulated the test time of the flow. The camera was set to have a 200 frame pre-trigger and was activated by a TTL pulse from the facility prior to the test. The schlieren mirrors were of 300 mm diameter and had a focal length of 1660 mm.

A FASTCAM UX100 high-speed camera with a 30 mm lens recorded the model movement directly for image tracking purposes. The camera faced directly through the test section windows, imaging the longitudinal plane of motion of the model. A frame rate of 4000 fps was used giving a resolution 1,280 x 1,024 pixels. Two LED bike lights were used to front light the model, producing sufficient light for the model to be well exposed. To fully capture the free-fall of the model, a pre-trigger of 800 frames was used and a total of 2180 frames recorded. A discussion of the image tracking technique is discussed in Section IV B.

The two cameras were positioned as such that both systems could operate concurrently during a test with neither system obstructing the field of view of the cameras.

IV. Data Analysis

Two non-intrusive techniques, on-board sensors and image tracking, were used to measure the kinematics of the model. The data reduction methods for both techniques are discussed below. Ultimately, the calculated linear and angular accelerations are used to calculate the aerodynamic coefficients according to Eq. (4), where the freestream dynamic pressure is calculated from the variables in Table 1, the mass and moment of inertia are taken from Table 2 and a reference area of S = 6.11x10^{-3} m^2 was used. The reference length used in the calculation of pitching moment was the model length. Calculation of the uncertainties is detailed in Appendix 1.

$$C_L = \frac{m\ddot{z}}{qS}, \quad C_D = \frac{m\ddot{x}}{qS}, \quad C_M = \frac{I_{yy}\ddot{\theta}}{qSc} \tag{4}$$

A. Processing IMU Data

Aerodynamic coefficients are conventionally measured relative to the oncoming flow, known as the stability axis. For wind tunnel experiments, this coincides with the Earth or Inertial frame which is defined as having the +z axis towards the ground, +x axis pointing upstream towards the facility nozzle and the +y axis orthogonal to both forming a right-hand coordinate system. During an experiment, the model and therefore IMU, rotate relative to the Earth frame of reference. Shown in Figure 5, the IMU data is thus recorded in a body fixed coordinate frame.

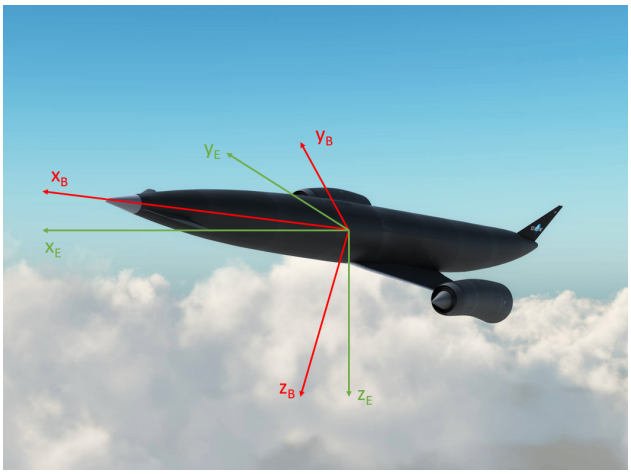

Fig. 5 Co-ordinate frames of reference (B is Body and E is Earth).

To convert the raw IMU data to aerodynamic coefficients, the following steps were taken. First, the data received from the on-board IMU was filtered using a 6^{th} order low pass Butterworth filter. The body-axis angular rates are then transformed to Euler-angle rates in the Earth axis through Eq. (5). This allows for the Euler angles to be determined through numerical integration of Euler-rates. Using these Euler angles, the measured linear accelerations are transformed from the body axes to the Earth axes using Eq. (6) so that lift and drag forces can be calculated.

The rotation matrix for the angular rates and accelerations are as follows (where c, s and t are cosine, sine and tangent functions respectively):

$$\begin{bmatrix} \dot{\phi} \\ \dot{\theta} \\ \dot{\psi} \end{bmatrix} = \begin{bmatrix} 1 & s(\phi)t(\theta) & c(\phi)t(\theta) \\ 0 & c(\phi) & -s(\phi) \\ 0 & \dfrac{s(\phi)}{c(\theta)} & \dfrac{c(\phi)}{c(\theta)} \end{bmatrix} \begin{bmatrix} p \\ q \\ r \end{bmatrix} \tag{5}$$

$$\begin{bmatrix} \ddot{X} \\ \ddot{Y} \\ \ddot{Z} \end{bmatrix}_E = \begin{bmatrix} c(\psi)c(\theta) & c(\psi)s(\phi)s(\theta) - c(\phi)s(\psi) & s(\phi)s(\psi) + c(\phi)c(\psi)s(\theta) \\ c(\theta)s(\psi) & c(\phi)c(\psi) + s(\phi)s(\psi)s(\theta) & c(\phi)s(\psi)s(\theta) - c(\psi)s(\phi) \\ -s(\theta) & c(\theta)s(\phi) & c(\phi)c(\theta) \end{bmatrix} \begin{bmatrix} \ddot{X} \\ \ddot{Y} \\ \ddot{z} \end{bmatrix} \tag{6}$$

Example filtered acceleration data in the Earth axes are presented in Fig. 6. As seen, the model free-falls for 120 ms before the onset of test flow, positioning the model at the nozzle centreline at flow start up. The facility has an approximately 40 ms start-up time in which the total pressure rises before reaching a plateau where the test time is taken. As seen in the figure the facility is timed so that only one plateau is produced, as after this time the model has moved out of the core flow and it reduces the likelihood of damage to the model.

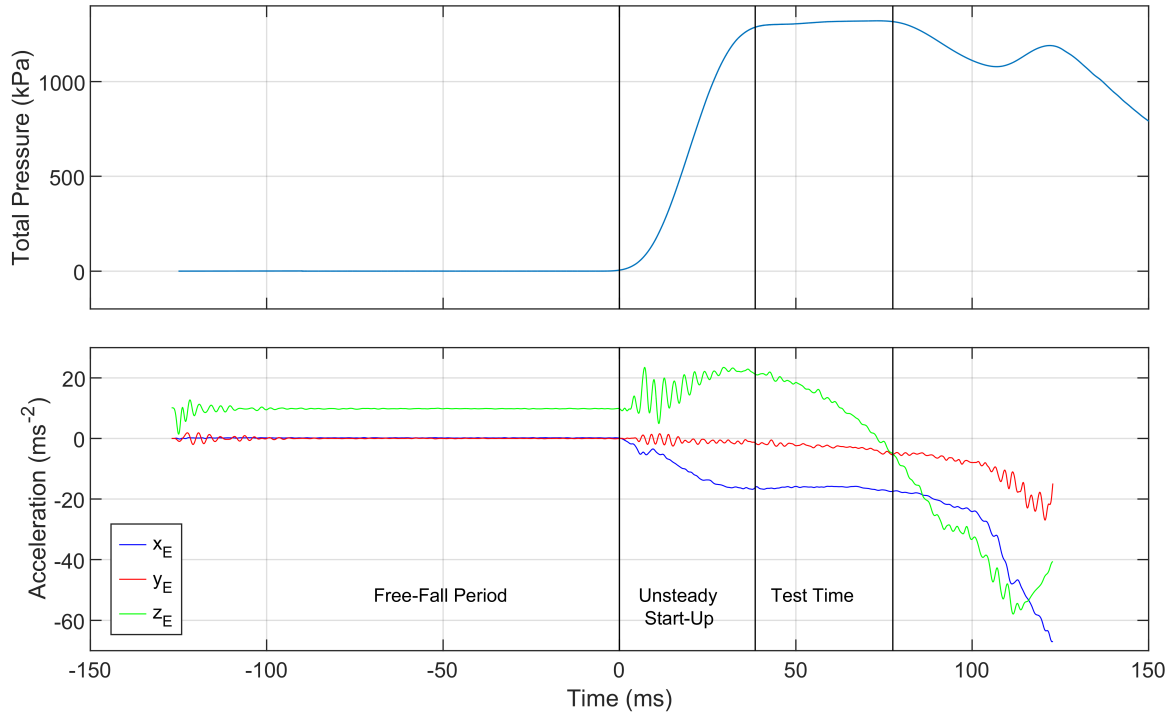

Fig. 6 Example filtered accelerometer accelerations in the Earth frame of reference with HDT total pressure.

B. Image Processing

Optical tracking to determine the model displacement used four black circles of known location, painted on the side of the model (Figure 4). Although only two circles are needed for data processing, additional circles provided redundancy in the event of low image contrast (a possible consequence of non-uniform lighting). The algorithm to determine the centre point of each circle for each video frame was as follows:

1) Apply Gaussian filter to image and subtract from original (High pass filter).
2) Apply Canny filter to image so that only pixels detected as an edge are shown [27].
3) Apply Hough transform to find circles in the image after narrowing the search radius [28].
4) Detect pixels in the proximity of the circle located by the Hough transform.
5) Use subpixel detection on the original image, at the location pixels were detected. Subpixel methodology set out in von Gioi [29].
6) Fit a circle to the pixels using linear regression as set out in Laurence *et al.* [14] and use this equation to find the centre point of the circle.

The centre of gravity and angle-of-attack are inferred by drawing a straight line between the centres of any two circles. Centre of gravity was measured prior to the test and was known relative to the circle locations. This process was repeated on each frame until the displacement (in pixels) of the centre of gravity and angle-of-attack history was obtained. As the distance between circles was known, the spatial resolution of the images can be found (0.54 mm/pixel) and used to determine actual displacement. The displacement of the model was differentiated twice to give accelerations and hence aerodynamic coefficients (Eq. (4)). The raw displacement data and intermediate velocity required smoothing before differentiation. Figure 7 shows an example of the image tracking for a test for which the model was close to the trim angle of attack. Prior to testing, the spatial uniformity of the lens was measured and corrected for through the use of a uniform grid inserted into the tunnel.

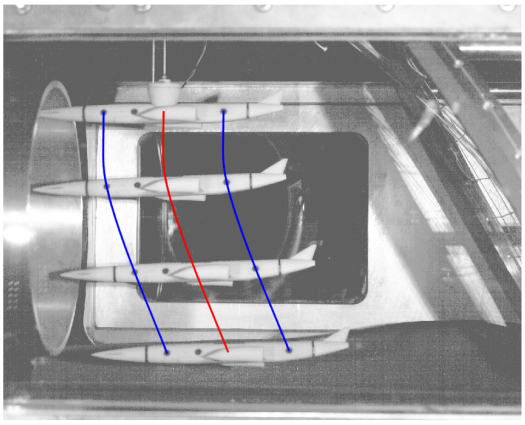

Fig. 7 Montage photo of image processing (Blue - detected circle centre points, Red - calculated centre of mass).

The performance of the algorithm was analysed by calculating the position of centre of gravity for 250 frames where the model was held stationary. The standard deviation of centre of gravity position for this test was calculated to be 41 μm. This is a very small standard deviation considering the spatial resolution of the pixels (0.54 mm/pixel) and the relative size of circles (radius of approximately 9.5 pixels) detected in relation to the rest of the frame (1,280 x 1,024 pixels.). This analysis does not take into account errors which come from misalignment of the optical equipment but gives an approximation of the uncertainty associated with the numerical algorithm.

V. Results

The results from the free-flight experiments are presented in this section. Lift, drag and pitching moment coefficients are calculated from the IMU data for four independent tests. Coefficients calculated from image tracking are also presented for a single shot. Finally, schlieren imagery is shown at the end of the section.

A. IMU Data

In total, four Skylon free-flight tests were conducted at the Mach 7 test condition. Figures 8 and 9 present lift and drag coefficient versus angle of attack measured by the accelerometers. Uncertainties are shown as shaded bands around the data points as calculated in Appendix 1 using the Taylor Series Method determining the propagation of uncertainties in freestream parameters, model properties and the IMU. Out of plane motion such as yaw was not included in the calculation of uncertainties. Data is also taken from Mehta *et al.* [6] and plotted on the figures.

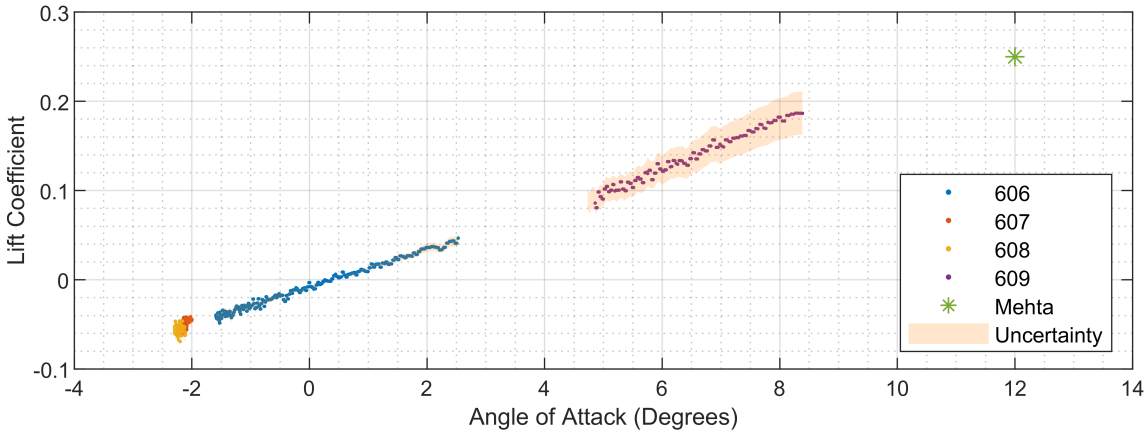

Fig. 8 Lift coefficient variation with angle of attack derived from the IMU data.

Lift coefficient, shown in Fig. 8, gives a linear trend with angle of attack, however, there is a slight increase in the gradient between shots 606 and 609. The lift coefficient is zero at approximately 0.27 ° angle of attack if a linear fit is chosen for the data. Extrapolating a linear fit to the data gives a lift coefficient of 0.26 ± 0.03 at 12 ° angle of attack. This compares well with the data from Mehta which is 0.25 at the same angle of attack.

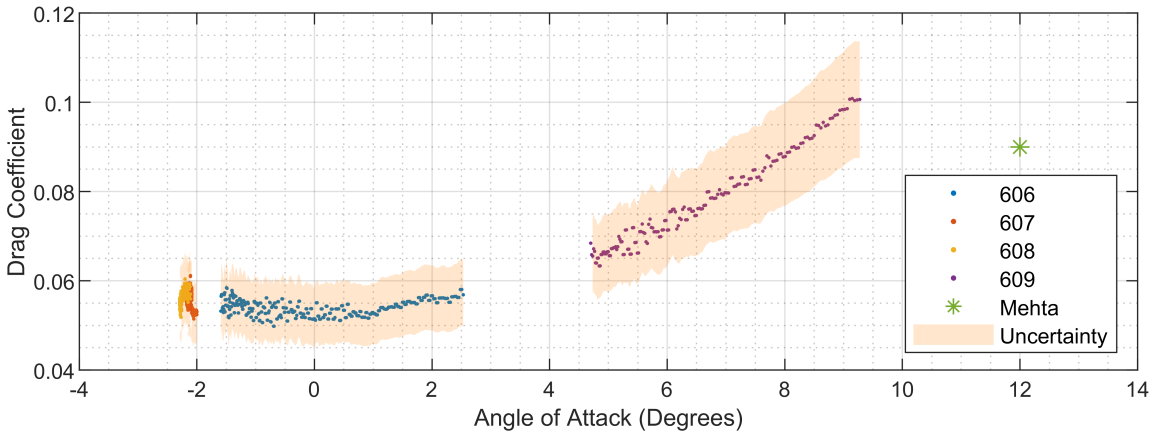

Fig. 9 Drag coefficient variation with angle of attack derived from the IMU data.

The data for drag coefficient is noisier than the data for lift coefficient. This is due to the sensitivity of model drag with respect to out-of-plane rotations such as yaw. The trend in drag coefficient was quadratic with a minimum occurring at 0.05 °. Extrapolating the trend in drag coefficient to alpha = 12 ° gives C_D = 0.133 ± 0.017; a result that is significantly higher than that of Mehta. This difference is seen because in the current work the model has sealed engine intakes, which inherently increase the drag. Furthermore, these tests were conducted at a Reynolds number over an order of magnitude lower than Mehta which increases the expected drag.

Shots 607 and 608 exhibit minimal pitching during the run with both being at a similar angle of attack. This suggests that the trim angle of attack is in the region of -2 to -2.4 °. This is further supported by Fig. 10 which presents the variation in pitching moment with angle of attack and has the zero pitching coefficient at a similar angle of attack. This data is inherently noisy due to the differentiation of the pitch rate data from the gyroscope to calculate angular acceleration for the pitching moment coefficient. In Fig. 10 the data is smoothed using a moving average filter. The data exhibits a general positive linear trend which implies static instability of the Skylon model. This agrees with motion seen in the footage for the tests in which the model pitches away from trim angle of attack when perturbed from equilibrium. Static instability is a common characteristic of vehicles with canards as increasing lift is generated near the front of the vehicle as angle of attack increases, which in turn increases the moment causing the vehicle to pitch (for a fixed canard angle). The small scale of the current model prevent the canards from being actively controlled as they would be on the real vehicle. Thus, the static instability could not be corrected during the test flow, resulting in the model sweeping through large range of angle of attack on some tests.

Figure 11 presents the lift-to-drag ratio for data recorded by the IMU. Initially the data increases linearly but the gradient decreases at higher angles of attack, eventually beginning to plateau at approximately 9 ° angle of attack. Testing at higher angles-of-attack was avoided due to the large lift generated and hence acceleration of the model to the top of the test section (which was not padded).

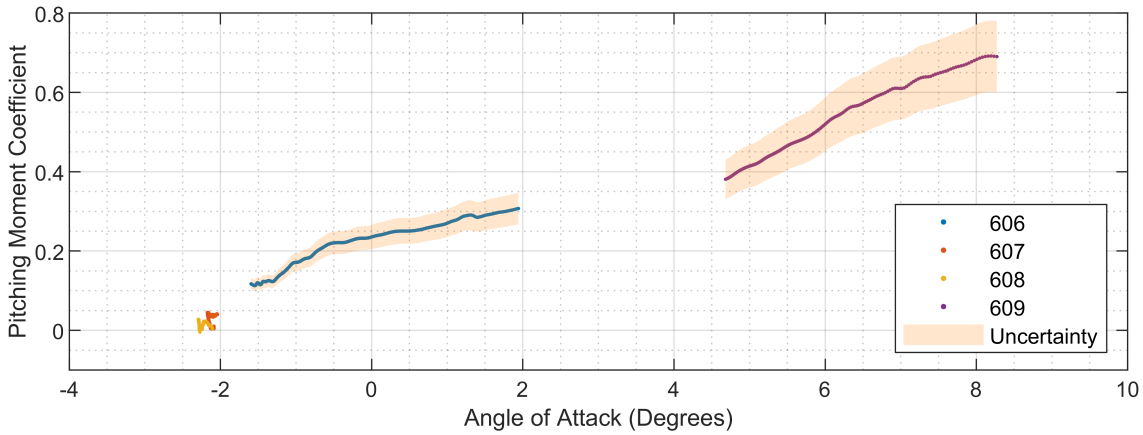

Fig. 10 Pitching Moment coefficient variation with angle of attack derived from the IMU data.

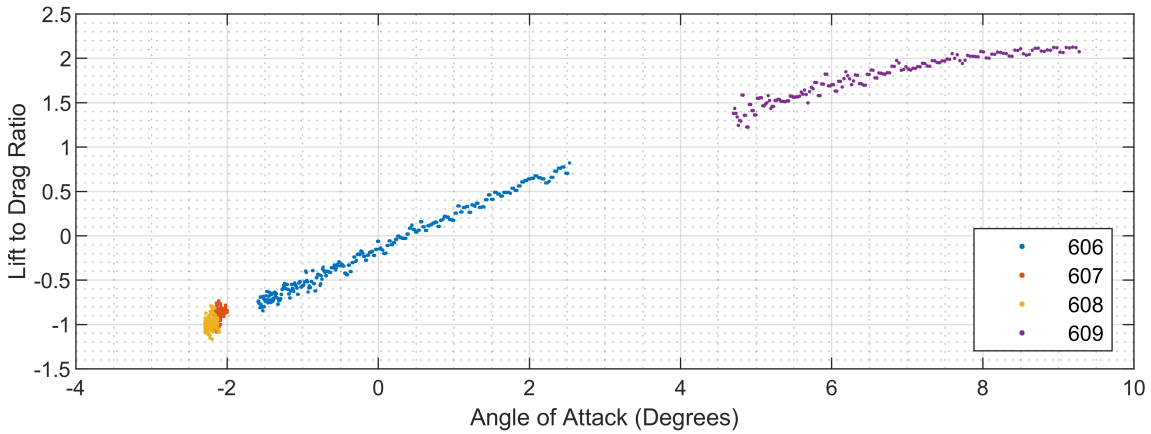

Fig. 11 Lift to Drag Ratio Lift variation with angle of attack derived from the IMU data.

B. IMU vs Image Processing

Figure 12 shows the aerodynamic coefficients from both methods, converted from their respective accelerations. The aerodynamic coefficients as measured through image processing show more scatter (approximately 5 times) due to the process of differentiation amplifying noise, even with smoothing. For lift coefficient there is an offset observed between the two methods which is attributed to the uncertainty in initial angle of attack of the model when released. As the calculation of angle of attack from angular velocities recorded by the gyroscopes requires knowledge of the initial conditions, any uncertainty in this value causes an offset in the whole entire set. Drag coefficient for image processing shows even greater scatter but overall compares well with the IMU data. Overall, it is still very useful to have both methods to measure coefficients as it gives some degree of validation to the results.

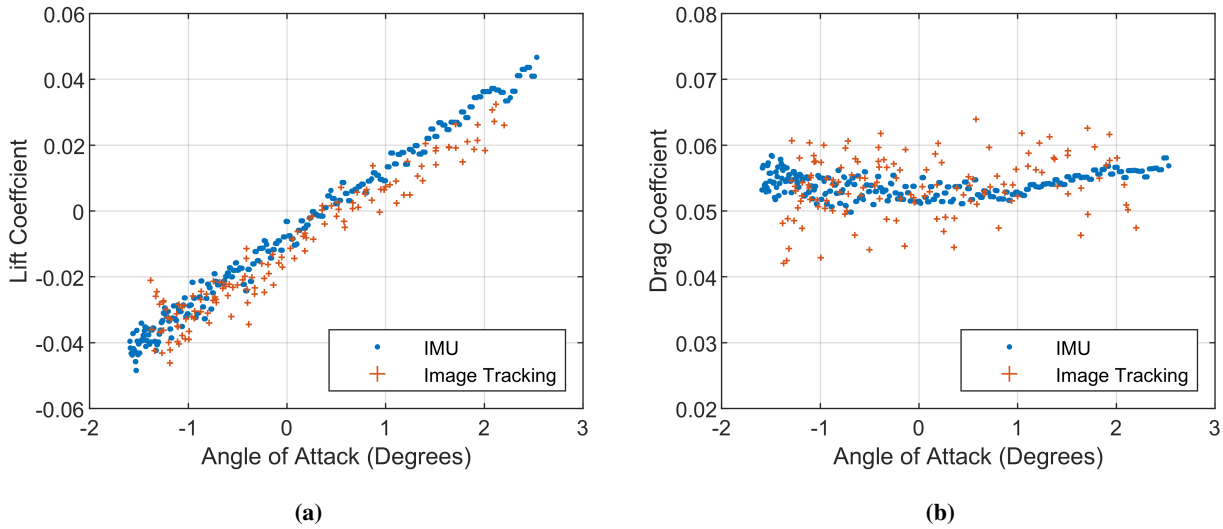

(a) **(b)**

Fig. 12 Comparison of lift (a) and drag (b) coefficient as measured by image tracking and on-board sensors for shot 606

C. Flow Visualisation

Schlieren was used to visualise the flow field around the model as it moved. Expansion and shock waves can clearly be seen throughout the course of a test. Unfortunately, the whole Skylon vehicle cannot be seen in one frame due to the limitation of mirror size at the facility and elliptical field of view. Figure 13 shows a series of images from a Skylon free-flight test and the model trajectory as determined derived by the IMU. As the test progresses and the model begins to pitch, the bow shock moves closer to the underside of the model.

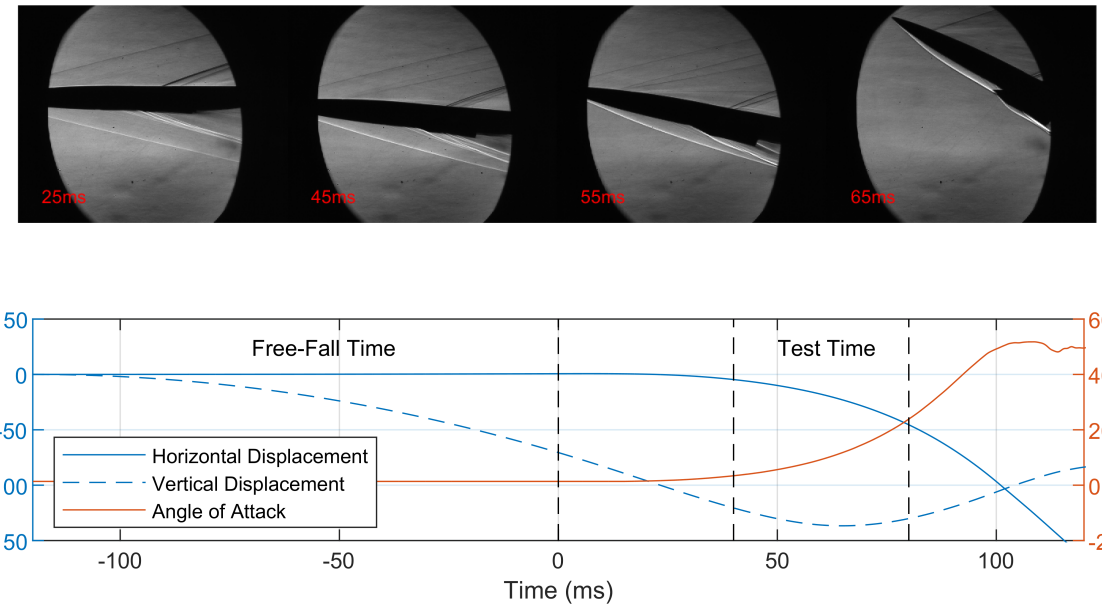

Fig. 13 Schlieren images and model trajectory determined from IMU for shot 609

VI. Conclusion

The experimental measurement of lift, drag and pitching moment have been presented for the Reaction Engines Skylon spaceplane for 4 independent shots at a Mach 7 test condition. Whilst the mass scaling requirements were not met in this campaign and the test conditions represented a higher altitude than the flight trajectory point, the results still gave useful insight into aerodynamic coefficients of the Skylon vehicle, which can be validated against numerical simulations. Lift and drag coefficient exhibited the expected shapes with respect to angle of attack and the gradient of pitching moment coefficient showed the vehicle to be statically unstable, which was clear from the test videos. This instability is an expected feature of the vehicle due to the lack of active control on the model with respect to the canards. Further research could be conducted to investigate what angle of attack of the canards is required to trim the vehicle and counteract the nose-up moment produced in these series of tests. To determine the dominant factor for the disagreement of drag coefficient against Mehta's numerical simulations, future experiments could be conducted at a higher Reynolds number or having flow-through inlets on the model. Coupling image tracking with on-board accelerations allows for independent validation of the model accelerations during a test. To conclude, the new infrastructure designed for free-flight experiments has allowed for successful tests in the Oxford High Density Tunnel with consistent data measured across different tests.

VII. Acknowledgments

The authors would like to acknowledge Dr. Chris Kennell for his advice on kick-starting free-flight experiments at the University of Oxford. We are also grateful for the tireless work of Mr C. Hambidge and Dr. T. Hermann in the operation of the HDT.

References

[1] Wuilbercq, R., Pescetelli, F., Minisci, E., and Brown, R. E., "Influence of Boundary Layer Transition on the Trajectory Optimisation of a Reusable Launch Vehicle," *19th AIAA International Space Planes and Hypersonic Systems and Technologies Conference*, 2014, p. 2362. https://doi.org/https://doi.org/10.2514/6.2014-2362.

[2] Stetson, K. F., "Hypersonic boundary-layer transition," *Advances in Hypersonics*, Springer, 1992, pp. 324–417.

[3] Phillips, W., and Cruz, C., "Hypersonic Aerodynamic Characteristics for Langley Test Technique Demonstrator," *11th Applied Aerodynamics Conference*, 1993, p. 3443. https://doi.org/https://doi.org/10.2514/6.1993-3443.

[4] Liu, S. K., "Numerical Simulation of Hypersonic Aerodynamics and the Computational Needs for the Design of an Aerospace Plane," Tech. rep., 1992.

[5] Longstaff, R., and Bond, A., "The Skylon Project," *17th AIAA International Space Planes and Hypersonic Systems and Technologies Conference*, 2011, p. 2244. https://doi.org/https://doi.org/10.2514/6.2011-2244.

[6] Mehta, U. B., Aftosmis, M. J., Bowles, J. V., and Pandya, S. A., "Skylon Aerodynamics and SABRE Plumes," *20th AIAA International Space Planes and Hypersonic Systems and Technologies Conference*, 2015, p. 3605. https://doi.org/https://doi.org/10.2514/6.2015-3605.

[7] Pick, G. S., "Sting Effects in Hypersonic Base Pressure Measurements," Tech. rep., TR AL-85, Dec. 1971, Naval Ship Research and Development Center , Bethesda, Md., 1971.

[8] Juhany, K. A., and Darji, A., "Force Measurement in a Ludwieg Tube Tunnel," *Journal of Spacecraft and Rockets*, Vol. 44, No. 1, 2007, pp. 88–93. https://doi.org/10.2514/1.21014.

[9] Chambers, J., *Modeling Flight NASA Latest Version: The Role of Dynamically Scaled Free Flight Models in Support of NASA Aerospace Programs.*, Vol. 3, 2015.

[10] Mudford, N. R., O'Byrne, S., Neely, A., Buttsworth, D., and Balage, S., "Hypersonic Wind-Tunnel Free-Flying Experiments with Onboard Instrumentation," *Journal of Spacecraft and Rockets*, 2015. https://doi.org/10.2514/1.A32887.

[11] Kennell, C., Neely, A. J., O'Byrne, S. B., and Buttsworth, D., "Measurement of Vehicle Stability Coefficients in Hypersonic Wind Tunnels," *20th AIAA International Space Planes and Hypersonic Systems and Technologies Conference*, 2015, p. 3690. https://doi.org/https://doi.org/10.2514/6.2015-3690.

[12] Kennell, C., Neely, A. J., Buttsworth, D. R., Choudhury, R., and Tahtali, M., "Free Flight Testing in Hypersonic Flows: HEXAFLY-INT EFTV," *54th AIAA Aerospace Sciences Meeting*, 2016, p. 1152. https://doi.org/https://doi.org/10.2514/6.2016-1152.

[13] Tanno, H., Komuro, T., Sato, K., and Katsuhiro, I., "Aerodynamic characteristics of Generic Test Models Under High-Temperature Real-Gas Condition in Free-Piston Shock Tunnel HIEST," *HiSST: International Conference on High-Speed Vehicle Science Technology*, Vol. HiSST: Int, 2018, pp. 1–11.

[14] Laurence, S. J., and Hornung, H. G., "Image-Based Force and Moment Measurement in Hypersonic Facilities," *Experiments in Fluids*, Vol. 46, No. 2, 2009, pp. 343–353.

[15] Wolowicz, C. H., Bowman, J. S., and Gilbert, W. P., "Similitude Requirements and Scaling Relationships as applied to Model Testing," Tech. Rep. 1435, NASA, 1979.

[16] McGilvray, M., Doherty, L. J., Neely, A. J., Pearce, R., and Ireland, P., "The Oxford High Density Tunnel," *20th AIAA International Space Planes and Hypersonic Systems and Technologies Conference*, 2015, p. 3548. https://doi.org/https://doi.org/10.2514/6.2015-3548.

[17] Wylie, S., Doherty, L., and McGilvray, M., "Commissioning of the Oxford High Density Tunnel (HDT) for Boundary Layer Instability Measurements at Mach 7," *2018 Fluid Dynamics Conference*, 2018, p. 3074. https://doi.org/https://doi.org/10.2514/6.2018-3074.

[18] Mellinger, G. R., "Design and Operation of the X-15 Hypersonic Research Airplane," Tech. rep., No. AGARD-288, Advisory Group for Aerospace Research and Development, 1960.

[19] Mutzman, R., and Murphy, S., "X-51 Development: A Chief Engineer's Perspective," *17th AIAA international space planes and hypersonic systems and technologies conference*, Vol. 13, 2011.

[20] Di Benedetto, S., Di Donato, M. P., Rispoli, A., Cardone, S., Riehmer, J., Steelant, J., and Vecchione, L., "HEXAFLY-INT Project: Design of a High Speed Flight Experiment," *Proceedings of ISHF*, 2017.

[21] Eussel, W. R., *Aerodynamic Design Data Book, Volume-I, Orbiter Vehicle SIS-1*, National Technical Information Service, 1980.

[22] Barthelemy, R., "The National Aero-Space Plane Program," *Maintainablity of Aerospace Systems Symposium*, 1989, p. 5053.

[23] Keyes, F. G., "A Summary of Viscosity and Heat-Conduction Data for He, A, H2, O2, CO, CO2, H2O, and air," *Transactions of the ASME*, Vol. 73, 1951, pp. 589–596.

[24] Sutherland, W., "The Viscosity of Gases and Molecular Force," *The London, Edinburgh, and Dublin Philosophical Magazine and Journal of Science*, Vol. 36, No. 223, 1893, pp. 507–531.

[25] Oceanic, U. S. N., Administration, A., and Force, U. S. A., *US standard atmosphere, 1976*, Vol. 76, National Oceanic and Atmospheric Administration, 1976.

[26] McQuellin, L. P., Kennell, C. M., Neely, A. J., Sytsma, M. J., Silvester, T., Choudhury, R., and Buttsworth, D. R., "Investigating endo-atmospheric separation of a hypersonic flyer-sustainer using wind tunnel based free-flight," *23rd AIAA International Space Planes and Hypersonic Systems and Technologies Conference, 2020*, 2020, pp. 1–24. https://doi.org/10.2514/6.2020-2451.

[27] Canny, J., "A Computational Approach to Edge Detection," *IEEE Transactions on Pattern Analysis and machine Intelligence*, Vol. PAMI-8, No. 6, 1986, pp. 679–698.

[28] Hough, P. V. C., "Method and Means for Recognizing Complex Patterns," , dec 1962.

[29] von Gioi, R. G., and Randall, G., "A Sub-Pixel Edge Detector: an Implementation of the Canny/Devernay Algorithm." *IPOL Journal*, Vol. 7, 2017, pp. 347–372.

[30] Coleman, H. W., and Steele, W. G., *Experimentation, Validation, and Uncertainty Analysis for Engineers*, John Wiley & Sons, 2018.

[31] Hermann, T., Mcgilvray, M., Hambidge, C., Doherty, L., and Buttsworth, D., "Total Temperature Measurements in the Oxford High Density Tunnel," *FAR Conference*, 2019. https://doi.org/https://doi.org/10.2514/1.21014.

Appendix 1: Aerodynamic Coefficient Uncertainty

For a comprehensive understanding of experimental results, quantification of experimental uncertainties is required. With regards to free-flight, there are many sources of uncertainty such as; flow conditions, model geometric and inertial properties, experimental setup and orientation of the model in the flow. For the following analysis, the Taylor Series Method (TSM) will be used to determine the propagation of uncertainties. The assumption is also made that roll and yaw

is negligible during a test to simplify the analysis. The following equation describes the propagation of the uncertainties in the measured variables into the overall uncertainty of the desired output (for a full derivation see Coleman [30]):

$$U_r = \left[\sum_{i=1}^{J} \left(\frac{\partial r}{\partial X_i} \right)^2 U_i^2 \right]^{\frac{1}{2}} \tag{7}$$

As discussed, the main outcome of the free-flight technique is the measurement of aerodynamic coefficients. Application of Equation 7 to Equation 4 for lift coefficient yields (the same analysis can be completed for drag and pitching moment):

$$U_{C_L}^2 = \left(\frac{\partial C_L}{\partial m} \right)^2 U_m^2 + \left(\frac{\partial C_L}{\partial \ddot{z}} \right)^2 U_{\ddot{z}}^2 + \left(\frac{\partial C_L}{\partial \rho_\infty} \right)^2 U_{\rho_\infty}^2 + \left(\frac{\partial C_L}{\partial U_\infty} \right)^2 U_{U_\infty}^2 + \left(\frac{\partial C_L}{\partial S} \right)^2 U_S^2 \tag{8}$$

However, the variables ρ_∞ and U_∞ are not measured directly in the tunnel. Both variables are derived properties from isentropic relations through the use of other measured variables. Therefore, these two variables require their own uncertainty analysis which propagate back to the lift coefficient uncertainty. The isentropic relations for freestream velocity and freestream density are as follows (the uncertainty in Mach number and total temperature have been obtained in previous studies):

$$U_\infty = M \sqrt{\frac{\gamma R T_0}{\left(1 + \frac{\gamma - 1}{2} M^2 \right)}} \tag{9}$$

$$\rho_\infty = \frac{P_0}{R T_0} \left(1 + \frac{\gamma - 1}{2} M^2 \right)^{-\frac{1}{\gamma - 1}} \tag{10}$$

Equation 9 shows that the freestream velocity is a function of total temperature and Mach number whereas density in Equation 10 is a function of the aforementioned as well as total pressure. The application of Equation 7 to these isentropic relations yields:

$$U_{U_\infty}^2 = \left(\frac{\partial U_\infty}{\partial M} \right)^2 U_M^2 + \left(\frac{\partial U_\infty}{\partial T_0} \right)^2 U_{T_0}^2 \tag{11}$$

$$U_{\rho_\infty}^2 = \left(\frac{\partial \rho_\infty}{\partial M} \right)^2 U_M^2 + \left(\frac{\partial \rho_\infty}{\partial T_0} \right)^2 U_{T_0}^2 + \left(\frac{\partial \rho_\infty}{\partial P_0} \right)^2 U_{P_0}^2 \tag{12}$$

The relevant partial differential equations which can be substituted into Equations 8, 11 and 12 can be found at the end of this appendix. This uncertainty analysis can be extended further with knowledge of the static and pitot pressure transducers used to determine the uncertainty in freestream Mach number in the HDT. Substitution of the partial derivatives in the appendix and dividing through by the variable of interest gives the following equations for

which the uncertainties are calculated from:

$$\left(\frac{U_{U_\infty}}{U_\infty}\right)^2 = \left(\frac{1}{\left(1+\frac{\gamma-1}{2}M^2\right)}\right)^2 \left(\frac{U_M}{M}\right)^2 + \frac{1}{4}\left(\frac{U_{T_0}}{T_0}\right)^2 \tag{13}$$

$$\left(\frac{U_{\rho_\infty}}{\rho_\infty}\right)^2 = \left(\frac{M^2}{\left(1+\frac{\gamma-1}{2}M^2\right)}\right)^2 \left(\frac{U_M}{M}\right)^2 + \left(\frac{U_{T_0}}{T_0}\right)^2 + \left(\frac{U_{P_0}}{P_0}\right)^2 \tag{14}$$

$$\left(\frac{U_{C_L}}{C_L}\right)^2 = \left(\frac{U_m}{m}\right)^2 + \left(\frac{U_{\ddot{z}}}{\ddot{z}}\right)^2 + \left(\frac{U_{\rho_\infty}}{\rho_\infty}\right)^2 + 4\left(\frac{U_{U_\infty}}{U_\infty}\right)^2 + \left(\frac{U_S}{S}\right)^2 \tag{15}$$

Table 3 summarises the uncertainty values used for this analysis as well as those calculated in Equations 13 and 14. Mach number and total temperature uncertainties are obtained from other test campaigns in the HDT as currently in the free-flight setup, these two variables are not measured. The uncertainty in stagnation pressure is calculated from the uncertainty in the pressure transducer used to measure it.

Table 3 Uncertainties in freestream variables

Variable	Uncertainty (%)
Mach Number	± 5
Total Temperature	± 8.7
Total Pressure	± 1.25
Freestream Velocity	± 4.37
Freestream Density	± 8.80

It can be seen that the major source of uncertainty in the freestream variables originates from the uncertainty in total temperature which propagates through to give a large uncertainty in freestream density. The HDT has a very strong transient increase in total temperature during the first plateau of a shot due to unsteady compression in the plenum upstream of the nozzle throat and as all free-flight testing occurs during this first plateau, it results in a large uncertainty in total temperature. For more details on total temperature in the HDT see Herman *et al.* [31].

Table 4 Uncertainties in model variables

Variable	Uncertainty
Acceleration	± 0.05 (ms^{-2})
Angular Velocity	± 0.005 $(degs^{-1})$
Mass	± $5x10^{-4}(kg)$
Reference Area	± $1.6x10^{-4}(m^2)$

With the information contained in Tables 3 and 4 it is possible to calculate the uncertainty in the aerodynamic

coefficients. A similar analysis to the above can be conducted to derive analogous equations for the uncertainty in drag and pitching moment coefficient. Therefore, the overall uncertainties in lift, drag and pitching moment coefficient are shown in the following table:

Table 5 Uncertainties in aerodynamic coefficients

Variable	Maximum Uncertainty (%)
Lift Coefficient	± 12.4
Drag Coefficient	± 12.5
Pitching Moment Coefficient	± 12.7

The following presents the partial derivatives calculated as part of the uncertainty analysis. Starting with lift coefficient:

$$\frac{\partial C_L}{\partial m} = \frac{\ddot{z}}{\frac{1}{2}\rho_\infty U_\infty^2 S} = \frac{C_L}{m} \tag{16}$$

$$\frac{\partial C_L}{\ddot{z}} = \frac{m}{\frac{1}{2}\rho_\infty U_\infty^2 S} = \frac{C_L}{\ddot{z}} \tag{17}$$

$$\frac{\partial C_L}{\partial \rho_\infty} = -\frac{m\ddot{z}}{\frac{1}{2}\rho_\infty^2 U_\infty^2 S} = -\frac{C_L}{\rho_\infty} \tag{18}$$

$$\frac{\partial C_L}{\partial U_\infty} = -\frac{m\ddot{z}}{\frac{1}{4}\rho_\infty U_\infty^3 S} = -\frac{2C_L}{U_\infty} \tag{19}$$

$$\frac{\partial C_L}{\partial S} = -\frac{m\ddot{z}}{\frac{1}{2}\rho_\infty U_\infty^2 S^2} = -\frac{C_L}{S} \tag{20}$$

Freestream Velocity:

$$\frac{\partial U_\infty}{\partial M} = \frac{\sqrt{\gamma R T_0}}{\left(1 + \frac{\gamma - 1}{2} M^2\right)^{\frac{3}{2}}} = \frac{1}{M} \frac{U_\infty}{\left(1 + \frac{\gamma - 1}{2} M^2\right)} \tag{21}$$

$$\frac{\partial U_\infty}{\partial T_0} = \frac{M}{2\sqrt{T_0}} \sqrt{\frac{\gamma R}{\left(1 + \frac{\gamma - 1}{2} M^2\right)}} = \frac{U_\infty}{2T_0} \tag{22}$$

Freestream Density:

$$\frac{\partial \rho_\infty}{\partial M} = \frac{-MP_0}{RT_0}\left(1+\frac{\gamma-1}{2}M^2\right)^{-\frac{\gamma}{\gamma-1}} = \frac{-M}{\left(1+\frac{\gamma-1}{2}M^2\right)}\rho_\infty \tag{23}$$

$$\frac{\partial \rho_\infty}{\partial T_0} = \frac{-P_0}{RT_0^2}\left(1+\frac{\gamma-1}{2}M^2\right)^{-\frac{1}{\gamma-1}} = -\frac{\rho_\infty}{T_0} \tag{24}$$

$$\frac{\partial \rho_\infty}{\partial P_0} = \frac{1}{RT_0}\left(1+\frac{\gamma-1}{2}M^2\right)^{-\frac{1}{\gamma-1}} = \frac{\rho_\infty}{P_0} \tag{25}$$